

Rewritable nanoscale oxide photodetector

Patrick Irvin,¹ Yanjun Ma,¹ Daniela F. Bogorin,¹ Cheng Cen,¹ Chung Wung Bark,² Chad M. Folkman,² Chang-Beom Eom,² and Jeremy Levy^{1,*}

¹Department of Physics and Astronomy, University of Pittsburgh, Pittsburgh, Pennsylvania 15260

²Department of Materials Science and Engineering, University of Wisconsin-Madison, Madison, Wisconsin 53706

(Dated: March 12, 2021)

Nanophotonic devices seek to generate, guide, and/or detect light using structures whose nanoscale dimensions are closely tied to their functionality.^{1,2} Semiconducting nanowires, grown with tailored optoelectronic properties, have been successfully placed into devices for a variety of applications.^{3–5} However, the integration of photonic nanostructures with electronic circuitry has always been one of the most challenging aspects of device development. Here we report the development of rewritable nanoscale photodetectors created at the interface between LaAlO_3 and SrTiO_3 . Nanowire junctions with characteristic dimensions 2–3 nm are created using a reversible AFM writing technique.^{6,7} These nanoscale devices exhibit a remarkably high gain for their size, in part because of the large electric fields produced in the gap region. The photoconductive response is gate-tunable and spans the visible-to-near-infrared regime. The ability to integrate rewritable nanoscale photodetectors with nanowires and transistors in a single materials platform foreshadows new families of integrated optoelectronic devices and applications.

The discovery of a quasi two-dimensional electron gas (q-2DEG) at the interface between insulating oxides⁸ has accelerated interest in oxide-based electronics.⁹ The interface between LaAlO_3 and SrTiO_3 undergoes an abrupt insulator-to-metal transition as a function of the number of LaAlO_3 layers;¹⁰ for structures at or near the critical thickness ($d_c = 3$ unit cells), the conductance becomes highly sensitive to applied electric fields.¹⁰ By applying the electric field locally using a conducting AFM probe, one can control this metal-insulator transition with resolution approaching one nanometer.^{6,7} Devices such as rectifying junctions¹¹ and transistors⁷ can be created, modified, and erased with extreme nanoscale precision. Additionally, as LaAlO_3 and SrTiO_3 are both wide-bandgap insulators they are essentially transparent at visible wavelengths, making it an interesting material system on which to search for photonic functionality.

In this letter we demonstrate the creation of nanophotonic devices at the $\text{LaAlO}_3/\text{SrTiO}_3$ interface using conducting-AFM lithography (Figure 1a). Oxide heterostructures, consisting of 3 unit cells of LaAlO_3 on TiO_2 -terminated SrTiO_3 (ref. 12), are grown by pulsed-laser deposition (see the Supplementary Information for details about growth conditions). Following contact to the interface with low-resistance Au electrodes, nanostructures are created at the $\text{LaAlO}_3/\text{SrTiO}_3$ interface by applying positive voltages to a conducting AFM tip. Nanoscale insulating gaps are formed by “cutting” these nanowires with a negatively-biased AFM tip that passes over the nanowire. Electronic nanostructures can be created with a

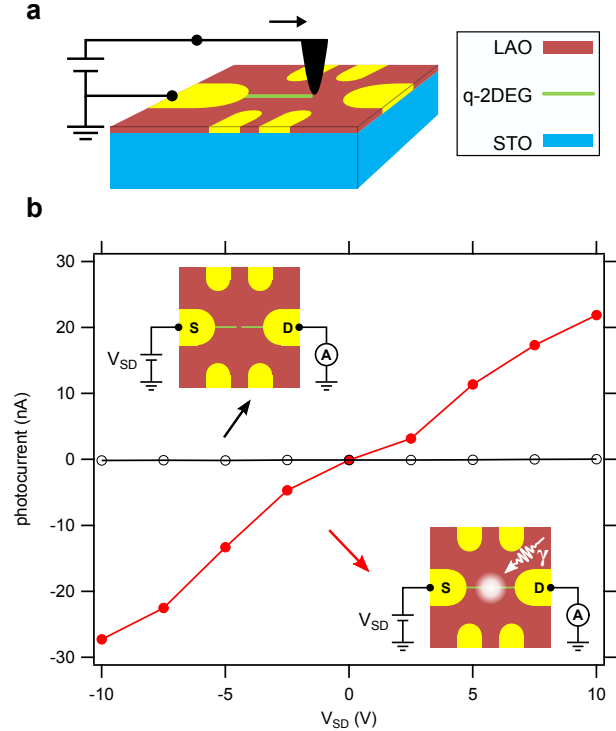


Figure 1. **Diagram of sample and photoresponse.** **a**, A schematic illustrating how a conducting atomic force microscope (AFM) tip writes a nanowire. **b**, Photocurrent vs. V_{SD} with (closed symbols) and without (open symbols) laser illumination. $I = 0.5 \text{ mW/cm}^2$ and $\lambda = 633 \text{ nm}$. $T = 300 \text{ K}$.

high degree of precision and, furthermore, are relocatable and reconfigurable.

The nanostructures are characterized by applying a voltage bias to a “source” electrode (V_{SD}) and then measuring the current from a “drain” electrode (I_D). Optical properties are measured by illuminating the sample with laser light; when the light overlaps with the device a sharp increase in the conductance is observed. A small, persistent photoconductive effect is observed under continuous illumination (Supplementary Figure 4). These background effects are removed by modulating the laser intensity at frequency f_R using an optical chopper. The resulting photocurrent, i_γ , is detected with a lock-in amplifier at f_R . Figure 1b shows a typical photocurrent response as a function of V_{SD} . The photoconductive properties of these nanodevices are mapped spatially using scanning photocurrent microscopy (SPCM).¹³ A microscope objective ($NA = 0.13$ or 0.73) mounted to a closed-loop, three axis piezo scanner focuses the light and raster-scans it relative to

the sample surface. The resulting photocurrent is measured as a function of laser position. To maximize nanostructure lifetimes,⁷ measurements are performed in a vacuum of < 1 mbar. To reduce the signal from thermally-activated carriers, some experiments are performed in a continuous-flow cryostat at $T = 80$ K.

The photosensitivity of the devices written at the $\text{LaAlO}_3/\text{SrTiO}_3$ interface is spatially localized near the gap regions. An SPCM image of the photocurrent between two electrodes that do not have a device written between them shows a spatially diffuse photocurrent of less than 2 pA (Figure 2a and Supplementary Figure 6). The simplest nanophotonic device consists of a nanowire with a narrow gap or junction. This device is created by first writing the wire with an AFM tip bias of $V_{tip} = +10$ V, producing a nanowire with width $w_w = 2.5$ nm (Supplementary Figure 1); the junction is created by crossing the wire with $V_{tip} = -10$ V, producing a gap with comparable width $w_j = 2.5$ nm. The nanowire junctions can be deterministically placed with nanometer-scale accuracy. The SPCM image shows localized photocurrent ($\lambda = 633$ nm and $T = 300$ K) detected in the region of the junction (Figure 2b). The devices are erasable and reconfigurable: after measuring the device shown in Figure 2b, the device was erased and a new device was created farther from the electrodes (Figure 2c). The photosensitivity of these devices can be optically modulated at frequencies as high as 3.5 kHz and the response appears to be limited by the RC time constant of the device (see the Supplementary Information).

More complex devices are readily created: a nanowire junction array (Figure 2d) consisting of seven parallel wires spaced $2 \mu\text{m}$ apart is drawn between the source and drain electrodes. The nanowires are subsequently cut in a single stroke using a tip bias of $V_{tip} = -10$ V, creating neighboring junctions of width $w_j = 2.5$ nm. The resulting photocurrent image shows the expected stripe shape, demonstrating that the photocurrent signal originates from all of the gaps. Even though the focused spot size ($\sim 0.5 \mu\text{m}$) is smaller than the line spacing, the individual junctions are not separately distinguished. The photocurrent at the interior junction is suppressed compared to the outermost junctions due to the electrical screening by the nanowires. This result indicates how carrier diffusion away from the junctions can also contribute significantly to the overall photocurrent response. The extent of the photoconductive spatial sensitivity appears to be of the order of the spacing in this case ($\sim 2 \mu\text{m}$).

The functionality of these devices can be extended by adding an independent gate electrode. Here, we adopt a geometry previously investigated as a nanoscale transistor, i.e., a “SketchFET”⁷. The “gate” electrode is written perpendicular to the existing source-drain nanowire (Supplementary Figure 2). This bias V_{GD} can be used to modify the source-drain conductance, enabling conduction between source and drain for positive V_{GD} and inhibiting it for negative V_{GD} . As for the two-terminal wire with junction, photocurrent that is spatially localized near the junction is observed where the device was written (Figure 3a). A simultaneously acquired laser reflectivity image (Figure 3b) does not show any observed signature of the nanophotonic detector, such as changes in the absorption

or scattering, which is also the case for two-terminal devices. SPCM images are acquired for an array of source and gate biases, $-5 \text{ V} \leq V_{SD}, V_{GD} \leq +5 \text{ V}$ (Supplementary Figure 5). The photocurrent, measured as a function of V_{SD} and V_{GD} (Figure 3c.) exhibits a polarity that is always the same sign as the V_{SD} , irrespective of V_{GD} , indicating that there is negligible leakage current from the gate to the drain. Furthermore, the photocurrent is suppressed when both V_{SD} is positive and V_{GD} is negative, demonstrating the ability of the gate electrode to tune the photoconductivity in the source-drain channel.

To investigate the wavelength dependence of these devices, a pulsed, mode-locked Ti:Sapphire laser is focused into a photonic crystal fiber to provide tunable laser illumination over the continuous wavelength range 600 – 1000 nm (ref. 14). As the white light source power varies with wavelength (Supplementary Figure 8) the normalized responsivity of the device (i_γ/P , where P is the laser power) is shown over this wavelength range (Figure 4). Data points in the vicinity of the pulsed laser source ($\lambda = 780$ nm) are not shown because of the high peak power and nonlinear effects in the sample (Figure 5). The spectral response is sensitive to V_{SD} and V_{GD} . At positive V_{SD} the photodetector response red-shifts as the gate bias is increased. The tuning of the responsivity is enhanced for positive V_{SD} , which is consistent with the behavior demonstrated in Figure 3. Measurements taken as a function of temperature (Supplementary Figure 9) show a slight red-shift with increasing temperature.

In addition to the supercontinuum white light source, the optical response is measured at a number of fixed wavelengths ranging from the visible to near-infrared: 532 nm, 633 nm, 735 nm, 1260 nm, and 1340 nm. The response at these wavelengths is consistent with the supercontinuum measurement in the range 600–1000 nm (Figure 5a). Remarkably, the photosensitivity extends to 1340 nm, the longest wavelength investigated. A three-terminal device has similar tuning behavior from V_{SD} and V_{GD} at 1340 nm and at visible wavelengths (Supplementary Figure 7). The intensity dependence of the photocurrent exhibits power-law behavior (Figure 5b), $i_\gamma = AI^m$, where i_γ is the photocurrent, A is a proportionality constant, I is the laser intensity, and $m \sim 1.2-1.4$. The super-linear scaling with laser intensity is similar to other systems that are near a metal-insulator transition.^{15,16}

There are several possible mechanisms for the photoconductivity. The direct and indirect bandgaps of SrTiO_3 (3.75 eV and 3.25 eV, respectively¹⁷) are too large to explain the visible to near-infrared photoresponse. Above-band photoexcitation of SrTiO_3 can produce excitonic luminescence at visible wavelengths, indicating the existence of mid-gap states.¹⁸⁻²⁰ The most readily formed mid-gap states are associated with oxygen vacancies, which are known to form during substrate preparation^{12,21,22} and growth of $\text{LaAlO}_3/\text{SrTiO}_3$ heterostructures.²³⁻²⁶ Localized states just below the conduction band have been probed via transport in SrTiO_3 -based field-effect devices.²⁷ Unintentional doping of SrTiO_3 substrates (e.g, Cr, Fe, or Al) can also contribute states within the bandgap.²⁸

Electrons occupying mid-gap states can be optically excited into the conduction band using sub-bandgap light. The pho-

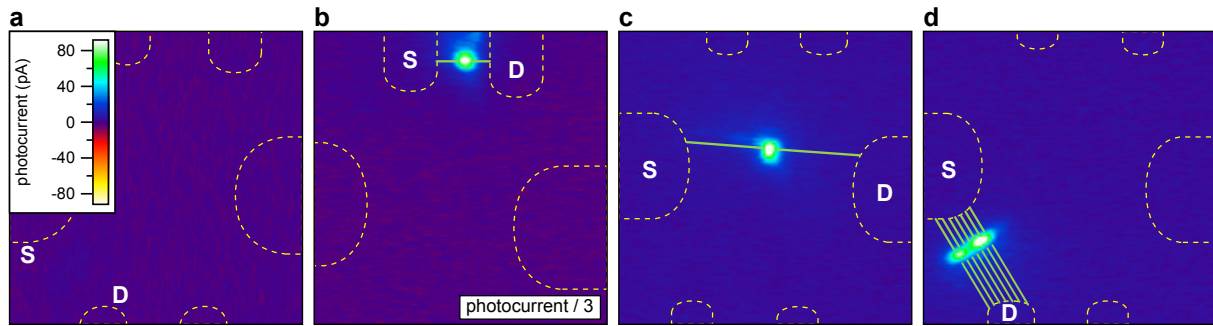


Figure 2. **Scanning photocurrent microscopy (SPCM) images of various nanostructures written at the $\text{LaAlO}_3/\text{SrTiO}_3$ interface.** Images are $50 \times 50 \mu\text{m}^2$. Dashed lines indicate boundaries of areas where electrical contact is made to the $\text{LaAlO}_3/\text{SrTiO}_3$ interface; solid lines indicate the locations of nanowires. **a**, SPCM image of area before any nanostructures are written. **b**, SPCM image for a nanowire junction written close to a pair of electrodes. **c**, SPCM image formed after erasing the previous nanowire and writing a second nanowire junction from the electrodes. **d**, SPCM image for a set of seven parallel wires with adjacent $w_j = 2.5 \text{ nm}$ gaps; the separation between each wire is $2 \mu\text{m}$. **a, b**, $I \sim 2.5 \text{ kW/cm}^2$, $V_{SD} = 0.5 \text{ V}$. **c, d**, $I \sim 3.8 \text{ kW/cm}^2$, $V_{SD} = 0.1 \text{ V}$. $T = 300 \text{ K}$.

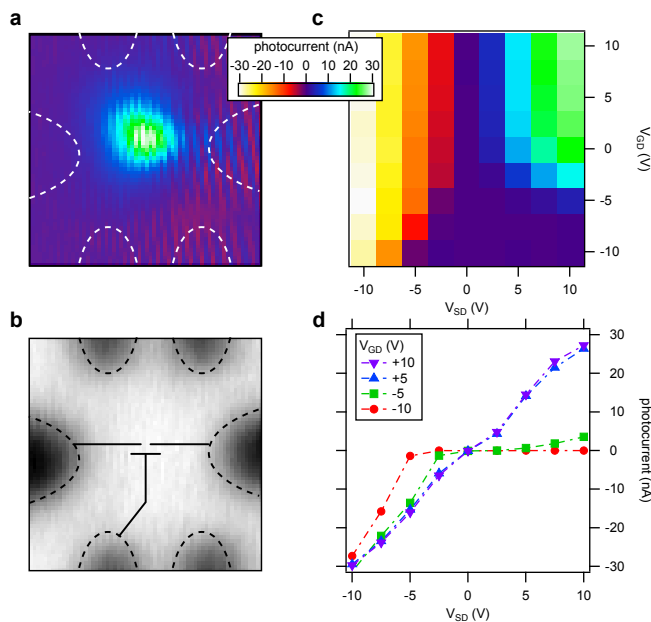


Figure 3. **Three-terminal, nanoscale, locally gateable photodetector.** **a**, SPCM image at $V_{SD}, V_{GD} = +10 \text{ V}$ and **b**, simultaneously acquired reflectivity image. The dashed lines show outline of electrodes and solid lines represent nanostructures written with an AFM. Both the nanowire widths and gap separations are exaggerated for clarity. Scan size is $50 \times 50 \mu\text{m}^2$. **c**, Photocurrent as a function of V_{SD} and V_{GD} . **d**, Photocurrent as a function of V_{SD} plotted for different values of V_{GD} . $I \sim 18 \text{ W/cm}^2$. $T = 80 \text{ K}$.

toexcited electrons are swept across the junction by the large electric field ($E = V_{SD}/w_j \sim 100 \text{ MV/cm}$), resulting in photocurrent. The spectral sensitivity we observe (Figures 4, 5, and Supplemental Figure 9) is consistent with previous optical measurements on oxygen vacancy-rich samples.^{21,22,24,26} Along the nanowire and sufficiently far from the gap, photo-induced current is negligible because the electric fields are screened or otherwise sufficiently small.

The rewritable photodetectors presented here bring new

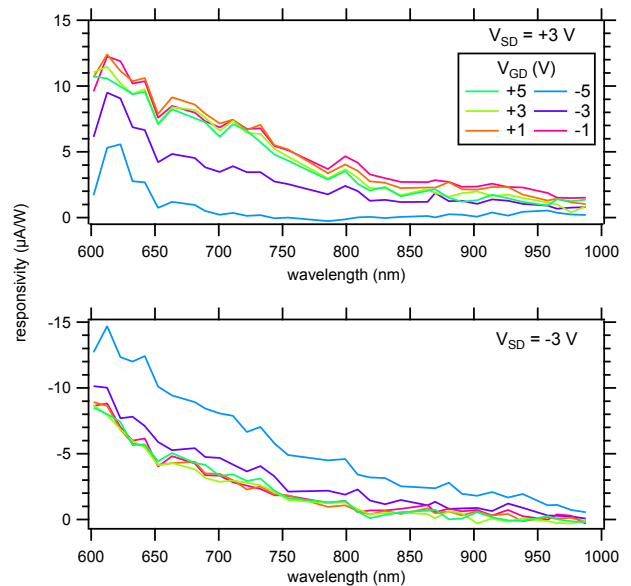


Figure 4. **Gate-controlled spectral response of photodetector.** Photocurrent as a function of λ and V_{GD} for $V_{SD} = +3 \text{ V}$ (top) and $V_{SD} = -3 \text{ V}$ (bottom). $T = 300 \text{ K}$.

functionality to oxide nanoelectronics. For example, existing nanowire-based molecular sensors²⁹ rely on the ability to bring the analyte into contact with the sensing area of the detector. Here the roles are reversed: a nanoscale photodetector can be placed in intimate contact with an existing molecule or biological agent. The ability to integrate optical and electrical components such as nanowires and transistors may lead to devices that combine in a single platform sub-wavelength optical detection with higher-level electronics-based information processing.

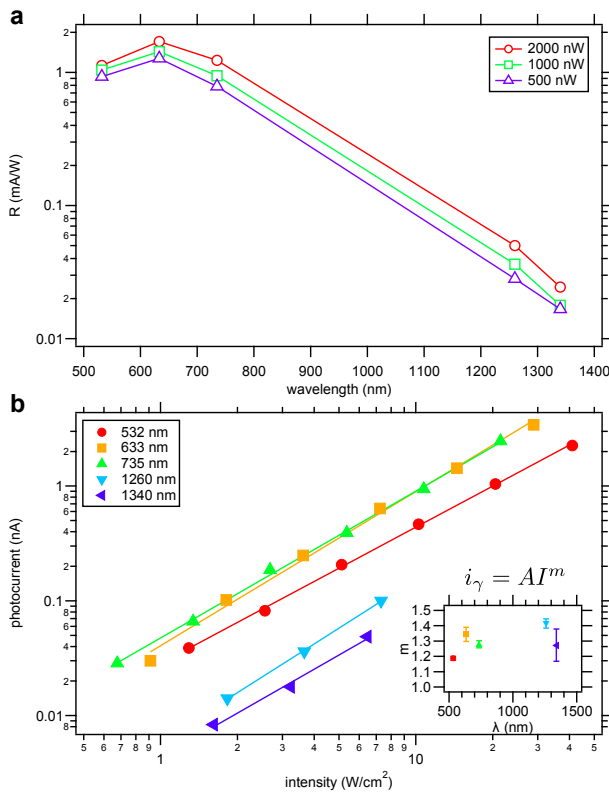


Figure 5. **Spectral sensitivity and intensity dependence from visible to near-infrared wavelengths.** **a**, Responsivity of photodetector from 532 nm to 1340 nm. **b**, Photocurrent versus optical intensity for different laser wavelengths. Symbols are data and lines are fits. The inset shows the power-law exponent m as a function of wavelength. $V_{SD} = 2$ V and $V_{GD} = 0$ V. $T = 80$ K.

ACKNOWLEDGMENTS

The authors gratefully acknowledge financial support from DARPA (W911N3-09-10258) (J.L.) the Fine Foundation (J.L.), and the National Science Foundation through grants DMR-0704022 (J.L.) and DMR-0906443 (C.B.E).

* jlevy@pitt.edu

- ¹ D. J. Sirbuly, M. Law, H. Yan, and P. Yang, *J. Phys. Chem. B* **109**, 15190 (2005).
- ² R. Agarwal and C. M. Lieber, *Appl. Phys. A: Mater.* **85**, 209 (2006).
- ³ J. Wang, M. S. Gudixsen, X. Duan, Y. Cui, and C. M. Lieber, *Science* **293**, 1455 (2001).
- ⁴ B. Tian, X. Zheng, T. J. Kempa, Y. Fang, N. Yu, G. Yu, J. Huang, and C. M. Lieber, *Nature* **449**, 885 (2007).
- ⁵ Z. Fan, J. C. Ho, Z. A. Jacobson, H. Razavi, and A. Javey, *P. Nat. Acad. Sci. (USA)* **105**, 11066 (2008).
- ⁶ C. Cen, S. Thiel, G. Hammerl, C. W. Schneider, K. E. Andersen, C. S. Hellberg, J. Mannhart, and J. Levy, *Nature Mater.* **7**, 298 (2008).
- ⁷ C. Cen, S. Thiel, J. Mannhart, and J. Levy, *Science* **323**, 1026 (2009).
- ⁸ A. Ohtomo and H. Y. Hwang, *Nature* **427**, 423 (2004).
- ⁹ J. Mannhart, D. Blank, H. Hwang, A. Millis, and J.-M. Triscone, *MRS Bull.* **33**, 1027 (2008).
- ¹⁰ S. Thiel, G. Hammerl, A. Schmehl, C. W. Schneider, and J. Mannhart, *Science* **313**, 1942 (2006).
- ¹¹ D. F. Bogorin, C. W. Bark, H. W. Jang, C. Cen, C.-B. Eom, and J. Levy, *Appl. Phys. Lett.* **97**, 013102 (2009), [arXiv:0912.3714v1](https://arxiv.org/abs/0912.3714v1).
- ¹² M. Kawasaki, K. Takahashi, T. Maeda, R. Tsuchiya, M. Shino-hara, O. Ishiyama, T. Yonezawa, M. Yoshimoto, and H. Koinuma, *Science* **266**, 1540 (1994).
- ¹³ K. Balasubramanian, M. Burghard, K. Kern, M. Scolari, and A. Mews, *Nano Lett.* **5**, 507 (2005).
- ¹⁴ J. M. Dudley, G. Genty, and S. Coen, *Rev. Mod. Phys.* **78**, 1135 (2006).
- ¹⁵ F. Stöckmann, *Phys. Stat. Sol.* **34**, 751 (1969).
- ¹⁶ S. Prezioso, S. M. Hossain, A. Anopchenko, L. Pavesi, M. Wang, G. Pucker, and P. Bellutti, *Appl. Phys. Lett.* **94**, 062108 (2009).
- ¹⁷ K. van Benthem, C. Elsasser, and R. H. French, *J. App. Phys.* **90**, 6156 (2001).
- ¹⁸ L. Grabner, *Phys. Rev.* **177**, 1315 (1969).
- ¹⁹ R. Leonelli and J. L. Brebner, *Phys. Rev. B* **33**, 8649 (1986).
- ²⁰ H. Okamura, M. Matsubara, K. Tanaka, K. Fukui, M. Terakami, H. Nakagawa, Y. Ikemoto, T. Moriwaki, H. Kimura, and T. Nanba, *J. Phys. Soc. Jpn.* **75**, 023703 (2006).
- ²¹ M. Kareev, S. Prosandeev, J. Liu, A. Kareev, J. W. Freeland, M. Xio, and J. Chakhalian, *Appl. Phys. Lett.* **93**, 061909 (2008).
- ²² J. Zhang, S. Walsh, C. Brooks, D. G. Schlom, and L. J. Brillson, *J. Vac. Sci. Technol. B* **26**, 1466 (2008).
- ²³ G. Herranz, M. BasletiĆ, M. Bibes, C. Carrétero, E. Taffra, E. Jacquet, K. Bouzouhane, C. Deranlot, A. Hamzić, J.-M. Broto, A. Barthélémy, and A. Fert, *Phys. Rev. Lett.* **98**, 216803 (2007).

- ²⁴ A. Kalabukhov, R. Gunnarsson, J. Borjesson, E. Olsson, T. Claesson, and D. Winkler, *Phys. Rev. B* **75**, 121404 (2007).
- ²⁵ M. Basletic, J. Maurice, C. Carretero, G. Herranz, O. Copie, M. Bibes, E. Jacquet, K. Bouzehouane, S. Fusil, and A. Barthelemy, *Nature Mater.* **7**, 621 (2008).
- ²⁶ S. S. A. Seo, Z. Marton, W. S. Choi, G. W. J. Hassink, D. H. A. Blank, H. Y. Hwang, T. W. Noh, T. Egami, and H. N. Lee, *Appl. Phys. Lett.* **95**, 082107 (2009).
- ²⁷ K. Shibuya, T. Ohnishi, T. Sato, and M. Lippmaa, *J. App. Phys.* **102**, 083713 (2007).
- ²⁸ T. Feng, *Phys. Rev. B* **25**, 627 (1982).
- ²⁹ Y. Cui, Q. Wei, H. Park, and C. M. Lieber, *Science* **293**, 1289 (2001).

Rewritable nanoscale oxide photodetector: Supplementary Information

Patrick Irvin,¹ Yanjun Ma,¹ Daniela F. Bogorin,¹ Cheng Cen,¹ Chung Wung Bark,² Chad M. Folkman,² Chang-Beom Eom,² and Jeremy Levy¹

¹*Department of Physics and Astronomy,
University of Pittsburgh, Pittsburgh, Pennsylvania 15260*

²*Department of Materials Science and Engineering,
University of Wisconsin-Madison, Madison, Wisconsin 53706*

MATERIAL GROWTH AND DEVICE PREPARATION

Oxide heterostructures are grown by pulsed laser deposition with in situ high pressure RHEED. Low miscut ($\sim 0.05^\circ$) (001) SrTiO₃ substrates are treated by a modified BHF etch and annealed in oxygen at 1000°C for 2 hours to produce a TiO₂-terminated and atomically smooth surface with single unit cell (uc) steps, as verified by AFM inspection. Thin (3 uc) layers of LaAlO₃ are deposited on SrTiO₃ at a temperature of 550 – 600°C and oxygen pressure of 10⁻³ mbar. A laser with energy density of 2 J/cm² and repetition rate of 3 Hz is used to ablate the LaAlO₃ single crystal target.

In order to probe the interface of LaAlO₃ and SrTiO₃, low-resistance electrodes are contacted directly to the q-2DEG. Argon ion beam etching is used to mill 25 nm deep into the SrTiO₃. Electrodes are then formed by first sputter-depositing a 2 nm Ti adhesion layer followed by 23 nm of Au into the etched region.

Wires with width $w_w \sim 2.5$ nm are written using an Asylum MFP-3D AFM in contact mode. A positive bias voltage applied to the tip creates conducting nanoregions directly below the AFM tip, while negative voltages locally restore the insulating state. Nanostructures are created under normal atmospheric conditions at room temperature; the AFM is kept in a dark environment to suppress photoconduction in the SrTiO₃ substrate ($E_g = 3.2$ eV). The conductivity of the q-2DEG is monitored with a Keithley picoammeter while writing: when the wire is connected to both electrodes, a sharp increase in conductance is observed. Similarly, the conductance is monitored while cutting a wire. The distance over which the conductance drops is used to quantify the wire width⁶, as shown in Supplementary Figure 1. Writing and erasing of nanowires is reproducible for a given tip bias and oxide heterostructure.

OPTICAL MODULATION

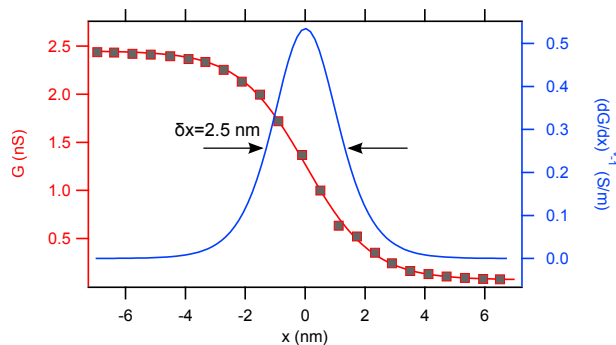
The photosensitivity of these devices can be optically modulated at frequencies as high as 3.5 kHz, as shown in Supplementary Figure 4. The phase of the photocurrent is constant over the frequency range probed while under illumination (ie, the “on” state). In this case the light lowers the resistance of the detector. The frequency response of the device is limited by the RC time constant of the junction. When the laser light is blocked (“off”), the detector is in a high resistance state. In the off state we observe a phase shift as the frequency is increased (Supplementary Figure 4), indicating we are indeed limited by the resistance.

SCANNING PHOTOCURRENT MICROSCOPY IMAGE ANALYSIS

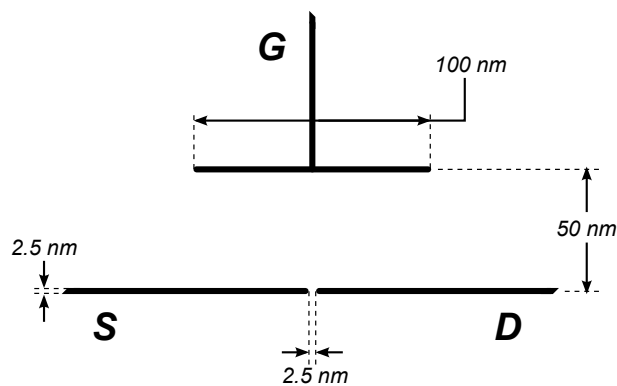
In order to extract a value for the photocurrent from a SPCM image, the image is fit to a two-dimensional Gaussian of the form

$$f(x, y) = A_0 + A_1 \exp\left\{(x - x_0)^2 / 2\sigma_x^2 + (y - y_0)^2 / 2\sigma_y^2\right\},$$

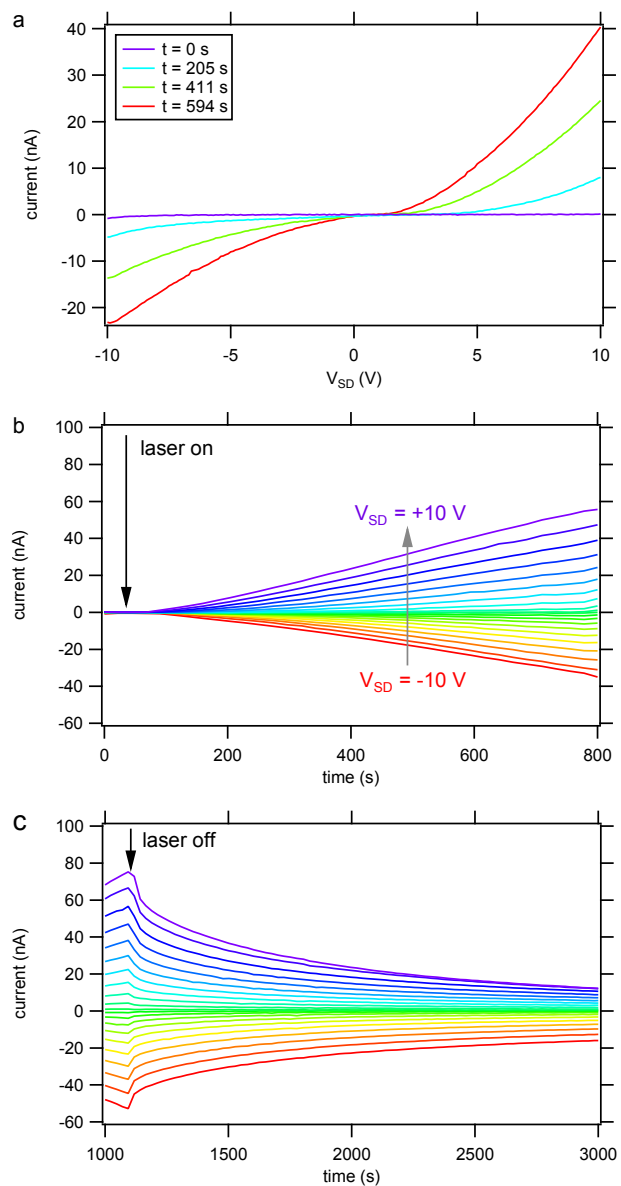
where A_0 is the image offset, A_1 is the amplitude of the 2D peak, x_0 and y_0 are the peak offsets, and σ_x and σ_y are the peak widths. We then define the photocurrent as $i_\gamma = A_1 - A_0$.



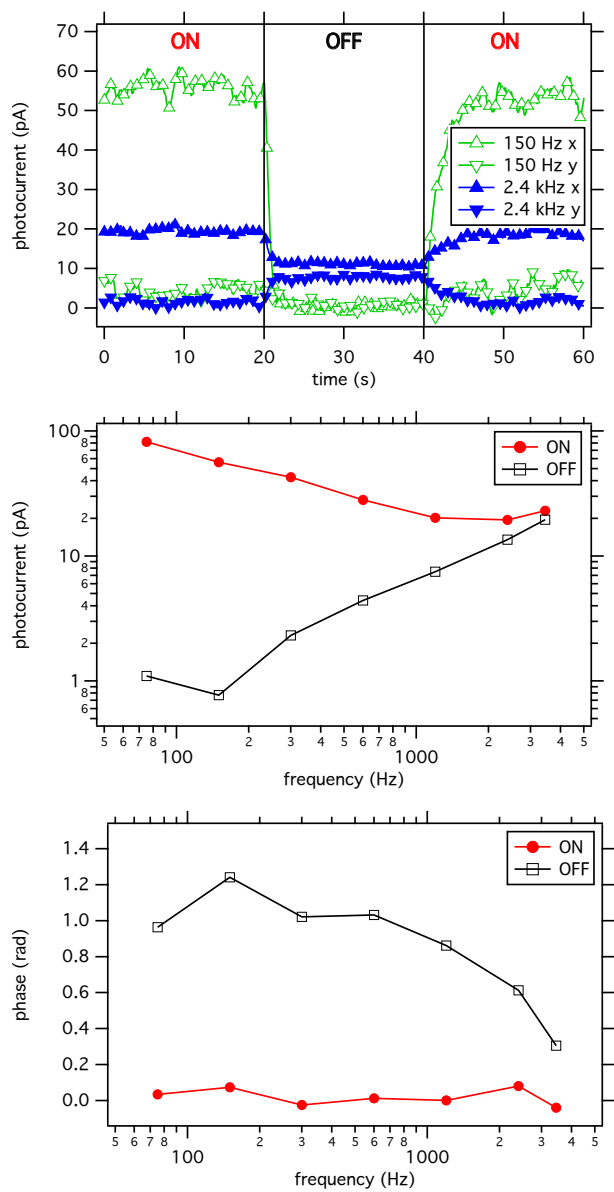
Supplementary Figure 1. **Width of wire.** Width of wire is determined by moving a reverse-biased tip across the wire while monitoring the conductance. The change in conductance is fitted to the function $G(x) = G_0 + G_1 \tanh(x/h)$. Also plotted is the deconvolved differential conductance $(dG/dx)^{-1}$, from which we determine the width of the nanowire.



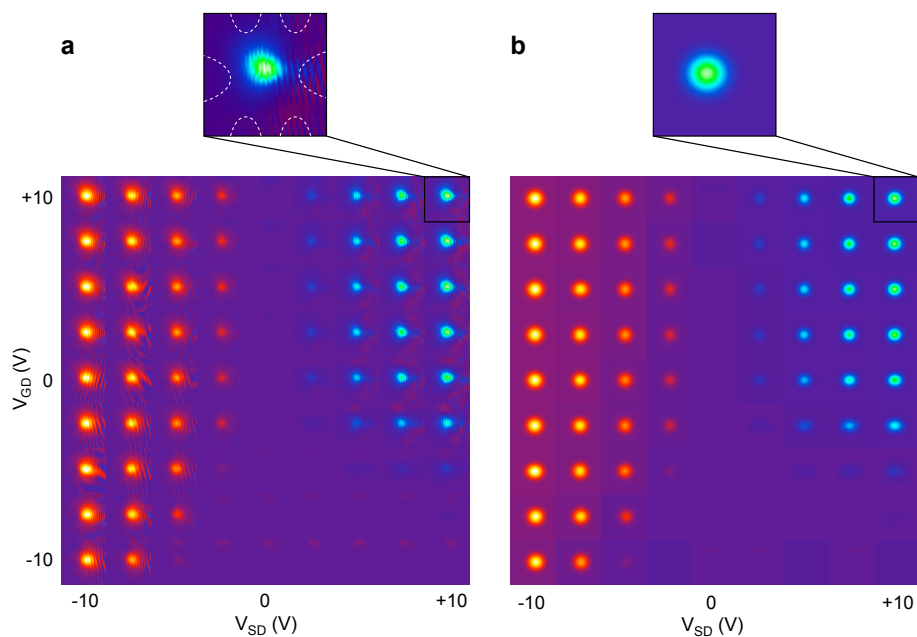
Supplementary Figure 2. **Nanophotonic detector geometry.** Typical geometry used for three-terminal devices. The source-drain junction width w_j is on the order of the size of the wire width, $w_w = 2.5$ nm. The gate electrode is positioned 50 nm from the source-drain wire. The “T” shape helps ensure a uniform electric field from the gate at the site of the junction.



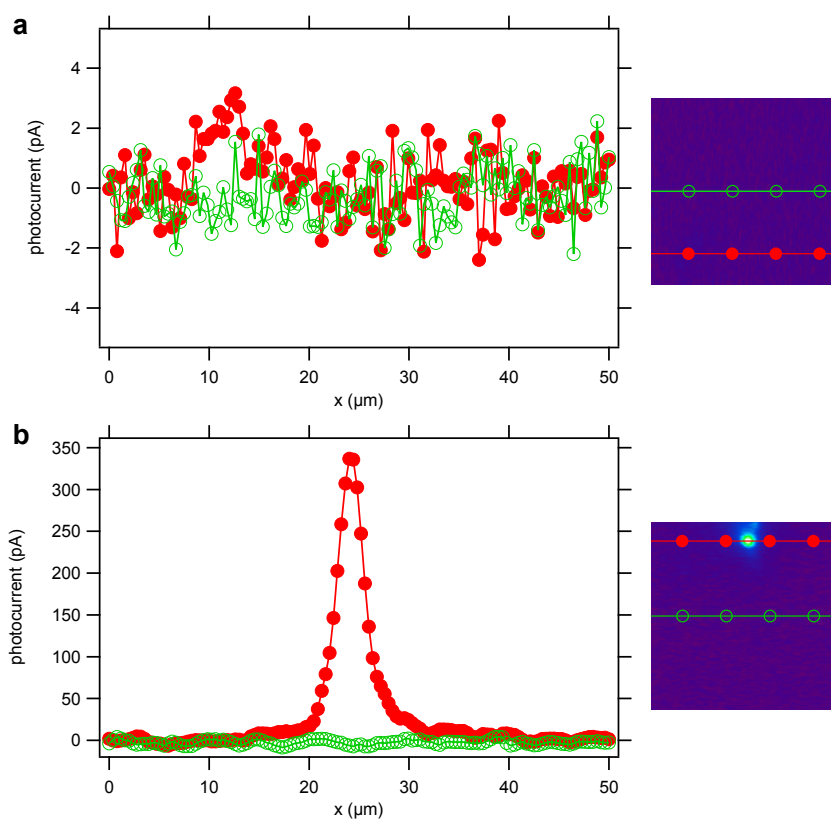
Supplementary Figure 3. **DC current vs. time.** **a**, DC current I_D plotted as a function of V_{SD} . Each curve is taken at a different time after turning on the laser illumination ($\lambda = 633$ nm, $I = 0.25$ mW/cm²). **b**, **c**, DC current as a function of time after laser is turned on (b) and off (c). Each curve represents a different V_{SD} . $T = 300$ K.



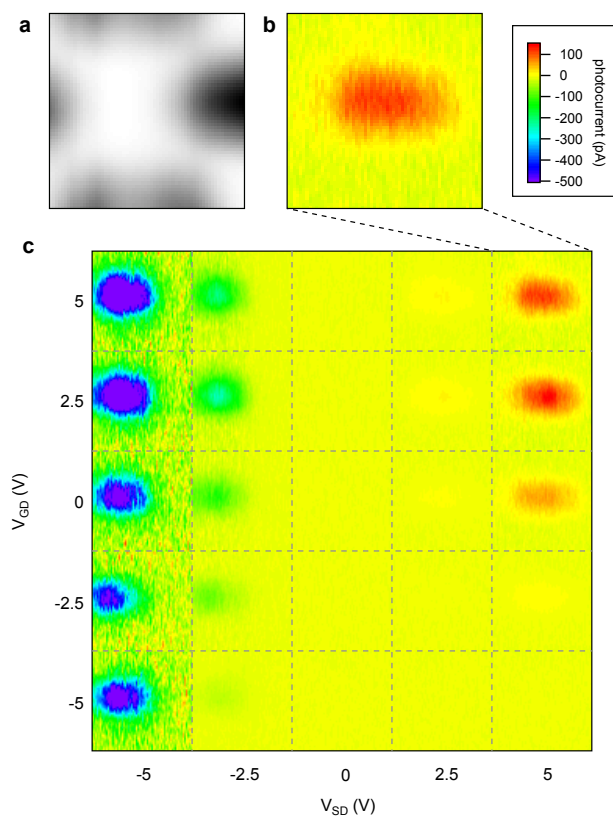
Supplementary Figure 4. **Switching photosensitivity vs. frequency.** **a**, Photocurrent versus time. Light that is initially on is blocked at $t = 20$ s and finally unblocked at $t = 40$ s. The light is intensity modulated by an optical chopper. Two modulation frequencies are shown: $f_R = 150$ Hz (open symbols) and $f_R = 2.4$ kHz (closed symbols). **b**, Photocurrent and **c**, Phase as a function of modulation frequency in the on and off states. $I \sim 0.5$ mW/cm². $T = 80$ K.



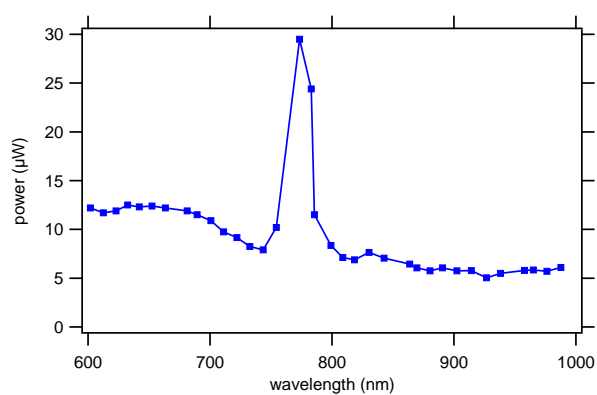
Supplementary Figure 5. **Three terminal device analysis.** **a**, Composite of SPCM images at different V_{SD} and V_{GD} . Inset shows SPCM image at V_{GD} , $V_{SD} = +10.5$ V. **b**, A 2D Gaussian fit is performed on the data. The amplitude minus a DC offset is plotted in Figures 3c and d.



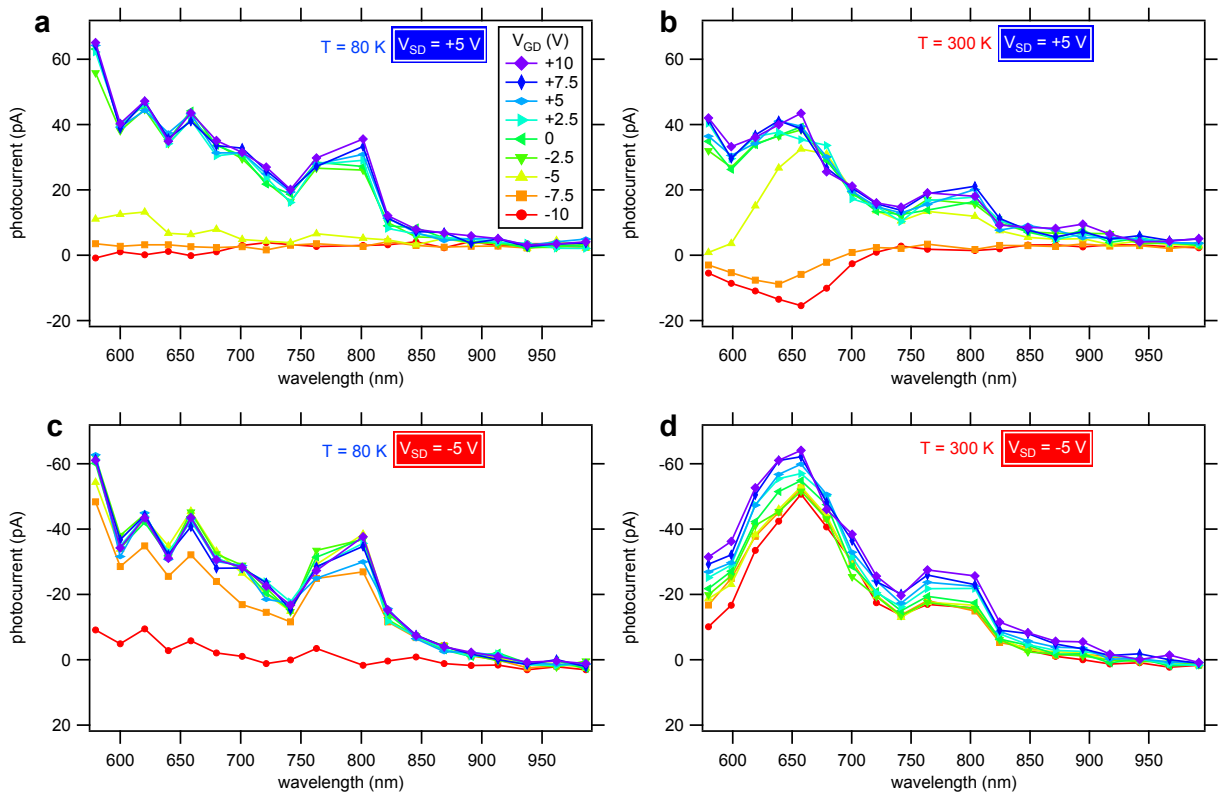
Supplementary Figure 6. **Nanophotonic device linecuts.** **a**, **b** Linecuts for the SPCM images shown in Figures 2a and b, respectively. The green curves (open symbols) show the signal away from the device while the red curves (closed symbols) show linecuts through the device. For the case where there is no device written (a), the red curve is drawn between the two electrodes that were used to measure the photocurrent.



Supplementary Figure 7. **Tuning the photoconductivity in the near-infrared.** **a**, Reflectivity image and **b**, simultaneously acquired SPCM image at $V_{SD}, V_{GD} = 10$ V. **c**, Composite image of SPCM images for an array of source and gate biases. $\lambda = 1340$ nm. $I \sim 4$ W/cm². Data taken at $T = 80$ K.



Supplementary Figure 8. **Supercontinuum laser power vs. wavelength.** Supercontinuum light is generated by focusing a pulsed, mode-locked Ti:Sapphire laser ($\lambda = 780$ nm, $\delta t_{pulse} = 150$ fs, $P = 0.5$ W) into a photonic crystal optical fiber. After exiting the fiber the light is filtered by a linear tunable bandpass filter mounted on a motorized linear translation stage.



Supplementary Figure 9. **Temperature dependence of spectral sensitivity.** Photocurrent plotted as a function of wavelength at different bias conditions. **a**, $T = 80 \text{ K}$, $V_{SD} = +5 \text{ V}$. **b**, $T = 300 \text{ K}$, $V_{SD} = +5 \text{ V}$. **c**, $T = 80 \text{ K}$, $V_{SD} = -5 \text{ V}$. **d**, $T = 300 \text{ K}$, $V_{SD} = -5 \text{ V}$. Laser power is shown in Supplementary Figure 8.